https://doi.org/10.5194/egusphere-2026-1499
Preprint. Discussion started: 1 April 2026


# Do GEMS geostationary satellite observations of tropospheric $NO_2$ always improve $NO_x$ emission estimates and related air quality modelling?

Fei Yao[1,2,3], Paul I. Palmer[2,3], Xiaolin Wang[4], Yi Wang[5], Gitaek T. Lee[6], Haolin Wang[3], Liang Feng[2,3], Daven K. Henze[7], and Rokjin J. Park[6]

[1]China-UK Low Carbon College, Shanghai Jiao Tong University, Shanghai 201306, China
[2]National Centre for Earth Observation, University of Edinburgh, Edinburgh EH9 3FF, United Kingdom
[3]School of GeoSciences, University of Edinburgh, Edinburgh EH9 3FF, United Kingdom
[4]School of Engineering and Applied Sciences, Harvard University, Cambridge, MA, USA
[5]Hubei Key Laboratory of Regional Ecology and Environmental Change, School of Geography and Information Engineering, China University of Geosciences, Wuhan 430074, China
[6]School of Earth and Environmental Science, Seoul National University, Seoul, Republic of Korea
[7]Department of Mechanical Engineering, University of Colorado, Boulder, CO 80309, USA

**Correspondence:** Fei Yao (fei.yao@sjtu.edu.cn) and Paul I. Palmer (paul.palmer@ed.ac.uk)

**Abstract.** Satellite observations of atmospheric composition from low Earth orbit (LEO) have significantly advanced our understanding of global tropospheric chemistry; however, their 12-hour overpass cadence limits the attribution of rapid compositional changes. The launch of the Korean Geostationary Environment Monitoring Spectrometer (GEMS) in 2020 heralded the beginning of continuous spaceborne monitoring of atmospheric composition during sunlit hours across Asia, allowing researchers to track atmospheric variability in real-time from a geostationary perspective. We assess the added value of GEMS observations of tropospheric $NO_2$ to estimate monthly emissions of $NO_x$ across Asia compared with the information provided by the equivalent instrument in LEO. We use the adjoint of the GEOS-Chem atmospheric chemistry transport model to infer $NO_x$ emissions, comparing estimates using the full set of GEMS tropospheric $NO_2$ data against a surrogate LEO dataset created by subsampling the GEMS data at 13:45 local time (Korea Standard Time, KST). We find that the benefits of assimilating high-frequency GEMS observations are most significant during non-summer months (September−May), when elevated $NO_2$ concentrations and pronounced diurnal variability provide strong constraints on emission estimates. During this period, $NO_x$ emission estimates derived from the full GEMS record deviate substantially from LEO-proxy results, with differences of 0.2−52.6 GgN month$^{-1}$, corresponding to 0.02−5.06% of the *a priori* emissions. These differences further propagate into widespread adjustments in modelled ozone, hydroxyl radicals, and other secondary species, with evaluation against independent *in situ* measurements showing that GEMS-inferred emission estimates offer comparable or superior performance particularly in regions where the differences are most pronounced. In contrast, we find that during summer months (June−August), low $NO_2$ levels likely introduce retrieval uncertainties that challenge the data assimilation framework in which only anthropogenic $NO_x$ sources are optimised, leading to negligible or even detrimental impacts on our ability to estimate $NO_x$ emissions.

https://doi.org/10.5194/egusphere-2026-1499
Preprint. Discussion started: 1 April 2026


## 1 Introduction

Widespread anthropogenic pollutant emissions pose a severe threat to public health across Asia, a region home to approximately 4.78 billion people – roughly 60% of the global population (HYDE (2023); Gapminder (2022); UN WPP (2024) – with major processing by Our World in Data). Effective air quality (AQ) management and mitigation strategies rely on the timely and accurate monitoring of these pollutant emissions. While conventional bottom-up inventories provide essential source-specific detail (Crippa et al., 2018; Hoesly et al., 2018; McDuffie et al., 2020; Crippa et al., 2023; Guizzardi et al., 2025), they are often hindered by reporting lags due to the labour-intensive nature of data collection. Top-down approaches, specifically satellite-based inverse modelling, offer a critical complementary framework by inferring emissions from real-time atmospheric observations (Wang et al., 2012; Xu et al., 2013; Wang et al., 2016, 2020; Cao et al., 2020). By integrating these two perspectives, researchers can generate the timely, actionable insights necessary for robust policy development and emission trend analysis.

Various spaceborne sensors provide the top-down observations necessary to constrain pollutant emission estimates through mathematical inverse modelling. Key instruments include the Moderate Resolution Imaging Spectroradiometer (MODIS) and the Multi-angle Imaging SpectroRadiometer (MISR) for aerosols (Wang et al., 2012; Xu et al., 2013); the Ozone Monitoring Instrument (OMI) and the Ozone Mapping and Profiler Suite (OMPS) for ozone, sulphur dioxide ($SO_2$), and nitrogen dioxide ($NO_2$) (Wang et al., 2016, 2020); and the Cross-track Infrared Sounder (CrIS) for ammonia ($NH_3$) (Cao et al., 2020). While newer platforms like the TROPOspheric Monitoring Instrument (TROPOMI) offer enhanced global distributions at higher spatial resolutions (Veefkind et al., 2012), these instruments are exclusively situated in low Earth orbit (LEO). This orbital configuration typically limits observations to two daily overpasses, roughly 12 hours apart. For sensors dependent on solar backscatter, only the daytime pass is viable, a window often further obscured by cloud cover. This restricted temporal sampling creates a critical data gap, hampering our ability to resolve diurnal cycles and accurately attribute pollutant variability to specific emission sources or meteorological processes.

Geostationary Earth orbit (GEO) instruments address the temporal limitations of LEO platforms by providing high-frequency, continuous observations of a fixed region, typically at sub-hourly intervals during sunlit hours. While this capability has been foundational to meteorological monitoring and aerosol science, facilitated by instruments such as the Geostationary Ocean Color Imager (GOCI) and the Advanced Himawari Imager (AHI) (Xu et al., 2015; Yeom et al., 2020; Letu et al., 2020; Choi et al., 2023), it has recently expanded to encompass a broader suite of trace gases. The 2020 launch of South Korea's Geostationary Environment Monitoring Spectrometer (GEMS) marked the advent of continuous spaceborne air quality monitoring (Choi et al., 2018; Kim et al., 2020). Combined with NASA's Tropospheric Emissions: Monitoring of Pollution (TEMPO) (Zoogman et al., 2017), launched in April 2023, and the European Space Agency's Sentinel-4 (Gulde et al., 2017), launched in July 2025, these sensors constitute the GEO AQ constellation. This international effort is expected to revolutionise our understanding of AQ variability and its underlying drivers, particularly over the densely populated regions of Asia, North America, and Europe.

https://doi.org/10.5194/egusphere-2026-1499
Preprint. Discussion started: 1 April 2026


As the first instrument of the GEO AQ constellation, GEMS provides hourly columnar loadings of ozone, aerosols, and key precursors ($NO_2$, sulphur dioxide ($SO_2$), formaldehyde (HCHO), and glyoxal (CHOCHO)) at a high spatial resolution. Despite the substantial volume of data accumulated since 2020, existing literature has focused predominantly on retrieval algorithms and validation (Kim et al., 2023; Lee et al., 2024; Seo et al., 2024), as well as the characterization of diurnal cycles (Yang et al., 2024; Edwards et al., 2024). The use of these data for top-down emission estimation remains under-explored. Early efforts by Xu et al. (2023) used an empirical approach for point sources that bypassed complex atmospheric processing. More recently, Park et al. (2024, 2025) employed a Bayesian framework to infer Asian $NO_x$ emissions, but their analysis was restricted to the winter−spring season of 2022 and species directly linked to $NO_x$. Consequently, it remains unclear how well geostationary $NO_2$ observations can infer $NO_x$ emission estimates and subsequent atmospheric chemistry, specifically ozone and aerosols, across a full annual cycle and varying seasonal photochemical regimes.

In this study, we quantify the added value of GEMS geostationary satellite observations of tropospheric $NO_2$ for constraining $NO_x$ emission estimates and to examine how this added value broadly influences our ability to model seasonal air pollutant distributions across the pan-Asian region from December 2020 to November 2021. We use the adjoint of the GEOS-Chem atmospheric chemistry transport model to infer $NO_x$ emission estimates from the full set of GEMS tropospheric $NO_2$ data and a temporal subsample of that data at 13:45 local time (Korea Standard Time) to represent a surrogate of LEO data. We use the latest GEMS v3.0 tropospheric $NO_2$ product, which incorporates corrected GEOS-Chem vertical coordinates for $NO_2$ shape factor calculations, resolving an issue identified in the previous v2.0 release (Oak et al., 2024). We analyse the spatiotemporal discrepancies and magnitude shifts between the two sets of inferred $NO_x$ emissions, and examine how these differences propagate across modelled atmospheric constituents, including $NO_2$, ozone, hydroxyl radicals (OH), carbon monoxide (CO), HCHO, $SO_2$, $NH_3$, and secondary inorganic aerosols (sulphate, ammonium, and nitrate). To validate the quantified added value of the geostationary observations, these modelled concentrations are benchmarked against independent *in situ* measurements.

The remainder of this paper is organized as follows: Section 2 details the GEOS-Chem adjoint model and the multi-source *in situ* datasets used for evaluation. Section 3 presents the inversion results for both the full GEMS dataset and the LEO proxy, evaluates their comparative performance, and discusses the implications for air quality modelling. Finally, Section 4 summarizes our findings and outlines future directions for GEMS data in atmospheric research.

## 2 Data and Methods

We first describe the GEMS v3.0 tropospheric $NO_2$ column data that we assimilate into the GEOS-Chem four-dimensional variational (4D-Var) data assimilation framework, including data screening and the characterization of error covariances. We then outline the 4D-Var framework and the experimental design that we have developed to quantify the added value of GEMS's high-frequency hourly sampling on emission constraints. Finally, we describe the suite of independent *in situ* measurements employed to evaluate the resulting chemical fields across the pan-Asian domain.

https://doi.org/10.5194/egusphere-2026-1499
Preprint. Discussion started: 1 April 2026


### 2.1 GEMS tropospheric $NO_2$ data as constraints

We use GEMS v3.0 Level-2 tropospheric $NO_2$ columns to infer $NO_x$ emission estimates over the pan-Asian region (50°–160°E, 10°S–55°N) from December 2020 to November 2021. Although the model domain extends beyond the GEMS field of view (75°–145°E, 5°S–45°N), atmospheric transport allows these observations to infer emission estimates both within and proximal to the satellite's footprint (Figure S1). As the first geostationary spectrometer of its kind, GEMS provides high-resolution hyperspectral measurements (300–500 nm; 0.6 nm full width half maximum) that enable the retrieval of multiple trace gases via Differential Optical Absorption Spectroscopy (DOAS) (Choi et al., 2018; Kim et al., 2020). This study focuses on $NO_2$ due to its direct link to $NO_x$ emissions, establishing a framework for future multi-species chemical data assimilation. As its v3.0 quality flags are still maturing, we found that restricting the inversion to "best-quality" flags (flag = 0) was overly conservative. Following consultation with the GEMS team, we adopted a broader selection filter − Solar Zenith Angle $< 70°$, Viewing Zenith Angle $< 70°$, and Cloud Fraction $< 0.3$ − to retain a robust dataset of approximately two billion retrievals. Data density peaks between 09:45 and 14:45 local time (Korea Standard Time, KST) and during the warm season (April−September), reflecting optimal solar geometry and longer daylight hours (Figure S2). Spatially, retrieval frequency is highest in the southeastern portion of the domain (Figures S3, S4).

In addition to tropospheric $NO_2$ column densities, the assimilation process requires two critical parameters: retrieval uncertainties and averaging kernels. The former characterises the observational error budget, while the latter describes the vertical sensitivity of the GEMS instrument to the true $NO_2$ profile.

The GEMS product includes a unitless "RootMeanSquareError" variable; however, this only captures the DOAS fitting error and does not represent the total observational uncertainty. While Lee et al. (2024) used this value, we follow the methodology of Yang et al. (2013, 2014) and Wang et al. (2020) to estimate the total uncertainty based on the standard deviation of retrievals within a pristine, pollution-free reference region. Although recommended by Boersma et al. (2007); Zara et al. (2018); Seo et al. (2024), the tropical Pacific (80°–130°E, 5°S–5°N) can be influenced by seasonal biomass burning from Southeast Asia (Marvin et al., 2024); therefore, we identify a stable reference region (100°–120°E, 20°–30°N; Figure S1) that is less influenced by major emission sources. The resulting estimated uncertainty of 0.0107 DU is comparable to the 0.011 DU reported for OMPS Level-2 data by Wang et al. (2020). While we acknowledge that pixel-level errors vary with cloud fraction, geometry, and aerosol loading, we adopt a uniform observation error of 0.0107 DU in the absence of analytical pixel-level estimates. To account for the uneven spatial distribution of GEMS observations (Figures S3, S4), we scale this uncertainty by the square root of the number of valid observations per model grid cell on a monthly basis (Wang et al., 2020). This adjustment ensures a spatially balanced cost function within the GEOS-Chem 4D-Var framework, as detailed in Section 2.2.

Regarding vertical sensitivity, the GEMS $NO_2$ product provides a 47-layer averaging kernel ($\mathbf{a}$), spanning the surface to 0.01 hPa. For our study, the troposphere is defined by layers below 230 hPa. The averaging kernel normalizes the scattering weights ($\mathbf{w}$) by the reported air mass factor (AMF) such that $a(z) = w(z)/\mathrm{AMF}$, where $z$ represents the vertical layer index. Following Fu et al. (2025), we interpolate the modelled $NO_2$ profiles to the GEMS vertical grid ($\mathbf{x_{comp}}$) and apply the kernels to derive

https://doi.org/10.5194/egusphere-2026-1499
Preprint. Discussion started: 1 April 2026


a model-equivalent tropospheric column ($c^{'}_{comp}$) that is directly comparable to the GEMS retrieval:

$$c^{'}_{comp} = \sum_{z} \mathbf{a}(z) \times \mathbf{x_{comp}}(z), \tag{1}$$

where $z$ goes from the surface to the tropopause. We acknowledge that while this process does not explicitly incorporate *a priori* profiles, the approach remains valid because the DOAS retrieval method does not rely on *a priori* information for slant column density estimation. Furthermore, the influence of *a priori* profiles in the slant-to-vertical column conversion is relatively limited compared to instruments using Bayesian optimal estimation, such as MOPITT (Deeter, 2002).

### 2.2 The GEOS-Chem model and its adjoint

The GEOS-Chem model (Bey et al., 2001) is a global 3-D chemical transport model driven by assimilated meteorological fields from the Goddard Earth Observing System (GEOS) of the NASA Global Modeling and Assimilation Office (GMAO). The GEOS-Chem adjoint model extends this forward simulation, providing a computationally efficient platform for calculating the sensitivity of a scalar cost function to a vast suite of model parameters (e.g., emissions) within a single backward integration (Henze et al., 2007, 2009). While these sensitivities can be used for direct sensitivity analysis, they are most often used within a 4D-Var data assimilation framework to optimize emission estimates, provided that the cost function is properly defined. To rigorously assess the added value of GEMS geostationary tropospheric $NO_2$ observations for $NO_x$ emission constraints and subsequent air quality modelling, we define the cost function ($J$) to be minimized as follows:

$$J = \frac{1}{2} \sum_{\boldsymbol{c} \in \Omega} \left( \boldsymbol{H}\boldsymbol{c} - \boldsymbol{c}_{obs} \right)^T \boldsymbol{S}_{obs}^{-1} \left( \boldsymbol{H}\boldsymbol{c} - \boldsymbol{c}_{obs} \right) + \frac{1}{2} \gamma_r \left( \boldsymbol{\sigma} - \boldsymbol{\sigma}_a \right)^T \boldsymbol{S}_a^{-1} \left( \boldsymbol{\sigma} - \boldsymbol{\sigma}_a \right), \tag{2}$$

where $\boldsymbol{c}$ is the vector of $c^{'}_{comp}$ mapped to the observation space by the observation operator $\boldsymbol{H}$; $\boldsymbol{c}_{obs}$ is the vector of GEMS tropospheric $NO_2$ retrievals; $\boldsymbol{S}_{obs}$ is the observation error covariance matrix; $\boldsymbol{\Omega}$ is the spatiotemporal domain over which modelled and observed tropospheric $NO_2$ are compared; $\boldsymbol{\sigma} = \ln(\mathbf{E}/\mathbf{E}_a)$ is the vector of logarithmic scaling factors for the $NO_x$ emissions, on which sensitivities are calculated and which are optimized by the quasi-Newton L-BFGS-B algorithm (Byrd et al., 1995), with $\mathbf{E}$ and $\mathbf{E}_a$ denoting the *a priori* and *a posteriori* $NO_x$ emissions, respectively; $\boldsymbol{\sigma}_a$ is the prior estimate of the parameter scaling factors (set to zero in this study, meaning that our initial guess for $\mathbf{E}$ equals $\mathbf{E}_a$); $\boldsymbol{S}_a$ is the error covariance estimate of the parameter scaling factors; and $\gamma_r$ is a regularization parameter that balances the relative weights of the observation and penalty terms in the cost function.

For each GEMS tropospheric $NO_2$ retrieval within the spatiotemporal domain $\boldsymbol{\Omega}$, spanning the pan-Asian region for each month from December 2020 to November 2021, the observation operator $\mathbf{H}$ identifies the corresponding model grid cell. The modelled value is then adjusted using the averaging kernels at the assimilation time step most proximal to the retrieval time. We assume the observation error covariance matrix, $\mathbf{S}obs$, is diagonal; the diagonal elements represent the total estimated uncertainty, scaled by observation density as detailed in Section 2.1, while the off-diagonal elements are set to zero, assuming spatially uncorrelated observation errors. The specification of the *a priori* error covariance matrix, $\mathbf{S}_a$, is contingent upon the emission inventories employed. Although recent versions of the GEOS-Chem forward model support a diverse array of state-of-the-science inventories, the adjoint model supports a more restricted subset. While 4D-Var inversions are primarily constrained

https://doi.org/10.5194/egusphere-2026-1499
Preprint. Discussion started: 1 April 2026


by atmospheric observations and are thus less sensitive to the initial *a priori* selection, utilizing contemporary emission inventories remains preferable to facilitate superior convergence during the optimization process (Tang et al., 2023). Following the implementation of aromatic chemistry and a suite of contemporary emission inventories into the GEOS-Chem adjoint by Wang et al. (2021), we extend those inventories to align with our study period. Anthropogenic emissions for China are derived from the Multi-resolution Emission Inventory for China (MEIC), updated to 2020 (Zheng et al., 2018, 2021), while the MIX-Asia inventory (Li et al., 2017) is applied to the remainder of the Asian domain. Global anthropogenic emissions outside of Asia are taken from the Community Emissions Data System (CEDS) (Hoesly et al., 2018). Biomass burning emissions are sourced from the Global Fire Emissions Database version 4.1 (GFED4s) (Van Der Werf et al., 2017), extended through 2021. Natural $NO_x$ precursors, including lightning (Price and Rind, 1992), soil (Yienger and Levy, 1995), and biogenic sources (Guenther et al., 2012), are calculated online within the GEOS-Chem framework. We assign an *a priori* uncertainty of 40% to anthropogenic emissions, representing a 2020 emission-weighted average of the uncertainties reported for MEIC and MIX-Asia (Li et al., 2017; Zheng et al., 2018). For non-anthropogenic emissions, we assign a broader uncertainty of 100%, consistent with previous inverse modeling studies across the pan-Asian region (Xu et al., 2013; Wang et al., 2020; Souri et al., 2020; Jung et al., 2022; Park et al., 2023, 2024, 2025). The *a priori* error covariance matrix, $\mathbf{S}_a$, is also assumed to be diagonal. This neglects spatial error correlations, a simplification justified by the fact that the correlation length scales of individual emission sources are typically smaller than the model's grid resolution (Stephen and Aneja, 2008). To further mitigate potential adverse effects of neglecting error correlations, we apply a regularization parameter ($\gamma_r$) to enforce a smoother solution. We set $\gamma_r$ to 10, a value identified as optimal through L-curve analysis in similar 4D-Var applications (Hansen, 1998; Henze et al., 2009).

While we acknowledge that the specifications for $\mathbf{S}_{obs}$, $\mathbf{S}_a$, and $\gamma_r$ entail inherent uncertainties, a comprehensive parameter sensitivity analysis is beyond the scope of this work. Instead, this study focuses on a relative assessment of the added value provided by geostationary sampling. By maintaining consistent parameter settings across our experimental suite, the contrast between inversions serves as a controlled metric for evaluating the impact of high-frequency observations. We distinguish between two primary experiments: a "GEMS-based" inversion using the full hourly dataset and a "LEO-proxy" inversion that serves as a surrogate for LEO instruments (e.g., OMI, OMPS, TROPOMI) by sub-setting observations to 13:45 local time (KST). For both cases, the cost function is minimized over ten iterations; we found that further iterations yielded marginal improvements, thus ten iterations represent an optimal balance between computational efficiency and convergence accuracy. The simulations are conducted at a global horizontal resolution of $2^\circ \times 2.5^\circ$ with 47 vertical layers, driven by GEOS-FP meteorological fields (1-hour temporal resolution for 2-D fields; 3-hour for 3-D fields) (Lucchesi, 2013). While nested-grid simulations at $0.25^\circ \times 0.3125^\circ$ are possible for sub-regions like China, the $2^\circ \times 2.5^\circ$ resolution was selected to ensure computational feasibility across the entire pan-Asian domain. Initial conditions were established via a long-term spin-up starting in January 2019 to eliminate the influence of initial state concentrations on the inversion results.

Following the updates to the GEOS-Chem adjoint framework, we perform a dual-phase evaluation of the model's performance. First, we execute a localized gradient consistency test by disabling horizontal transport processes. Under this configuration, the sensitivity of the observational cost function (excluding the regularization term) within an individual grid cell with respect to the local emission scaling factor ($\boldsymbol{\sigma}$) becomes mathematically equivalent to the total sensitivity across the entire

https://doi.org/10.5194/egusphere-2026-1499
Preprint. Discussion started: 1 April 2026


domain. This simplification allows for a direct, grid-by-grid comparison between sensitivities derived from the adjoint method and those calculated via the finite difference method. We verify the numerical accuracy of the adjoint-based gradients by using the finite difference results as a benchmark:

$$\wedge = \frac{J_{obs}(\boldsymbol{\sigma} + \delta\boldsymbol{\sigma}) - J_{obs}(\boldsymbol{\sigma} - \delta\boldsymbol{\sigma})}{2\delta\boldsymbol{\sigma}}, \tag{3}$$

where $J_{obs}$ is the observation part of the cost function. We adopt a perturbation of $\delta\boldsymbol{\sigma} = 0.01$ to calculate the finite-difference gradients, a value found to optimally balance truncation and round-off errors (Henze et al., 2009).

Second, we evaluate the internal consistency of the inversion by comparing modelled tropospheric $NO_2$ columns against the GEMS retrievals both before (*a priori*) and after (*a posteriori*) the optimization. While this assessment is not independent of the assimilation process, it serves as a critical diagnostic to verify that the 4D-Var framework effectively minimizes the model-observation mismatch and that the adjoint system is functioning as intended.

### 2.3 Experimental design

To reiterate, we conduct two distinct 4D-Var inversion experiments for each month from December 2020 to November 2021 across the pan-Asian region to rigorously quantify the added value of geostationary sampling for $NO_x$ emission constraints and subsequent air quality modelling:

- **GEMS-based inversion:** This experiment assimilates the full temporal suite of GEMS tropospheric $NO_2$ retrievals, leveraging the high-frequency diurnal sampling inherent to geostationary observations.
- **LEO-proxy inversion:** This experiment utilizes a subset of GEMS retrievals restricted to 13:45 local time (KST). This serves as a surrogate for LEO instruments (e.g., TROPOMI, OMI, and OMPS) which provide only a single daily overpass.

Both inversions use identical *a priori* emissions, model configurations, and cost function parameter settings. The optimization is achieved through ten iterations of the forward and adjoint model integrations. We evaluate the impact of hourly sampling by comparing the spatiotemporal distribution and magnitude of the resulting *a posteriori* $NO_x$ emissions. Furthermore, we examine the sensitivity of related chemical species, including $O_3$, OH, CO, HCHO, $SO_2$, $NH_3$, and secondary inorganic aerosols (sulfate, nitrate, and ammonium), to the different emission constraints. To validate the quantified added value of GEMS data, the modelled atmospheric constituents are evaluated against independent *in situ* measurements. Detailed descriptions of these independent datasets are provided below.

### 2.4 *In situ* measurements for independent assessment

To evaluate the chemical propagation of $NO_x$ emissions inferred from the "GEMS-based" and "LEO-proxy" inversions, we employ a diverse suite of independent *in situ* measurements. Hourly measurements of surface concentrations of $NO_2$, $O_3$, CO, $SO_2$, $NH_3$, and fine and coarse particulate matter are obtained from four national monitoring networks: the China National Environmental Monitoring Center (CNEMC), AirKorea, the Environmental Observatory of the National Institute for

https://doi.org/10.5194/egusphere-2026-1499
Preprint. Discussion started: 1 April 2026


Environmental Studies (Japan), and the Central Pollution Control Board (India). Due to varying reporting standards across these networks, modelled outputs are converted to the respective reported units and evaluated separately for each network. The spatial distribution of these surface monitoring stations is illustrated in Figure S1. For vertical column validation, we use high-frequency measurements from the Aerosol Robotic Network (AERONET) and the Pandonia Global Network (PGN). While AERONET is primarily recognized for aerosol characterization, it provides valuable columnar $NO_2$ and $O_3$ at intervals up to 15 minutes; 94 AERONET sites are available within our domain (Figure S1). We complement these data with columnar $NO_2$ from seven PGN sites, which offer sampling frequencies as high as every 2 minutes. To ensure data robustness and computational efficiency, we retain only PGN retrievals with the highest quality flag (flag = 0) and aggregate them into hourly averages for comparison with the model.

To rigorously evaluate the modelled atmospheric constituents against *in situ* measurements, we sample the model at the exact time and location of each observation. These paired data are then compiled into GEOS-Chem grid composites across multiple temporal scales: the afternoon overpass at 13:45 local time (KST), daytime averages (07:45 to 16:45 KST), and full daily averages. This multi-temporal approach allows for a comprehensive assessment of model performance driven by $NO_x$ emissions inferred from the "GEMS-based" and "LEO-proxy" inversions. To quantify the agreement between modelled and measured values, we employ a suite of geometrically related statistical metrics, including the Pearson correlation coefficient ($R$), normalised standard deviation (NSD), and normalised centralised root-mean-square error (NRMSE), defined as follows:

$$R = \frac{\sum_{i=1}^{N}(M_i-\overline{M})(O_i-\overline{O})}{\sqrt{\sum_{i=1}^{N}(M_i-\overline{M})^2}\sqrt{\sum_{i=1}^{N}(O_i-\overline{O})^2}}, \tag{4}$$

$$\mathrm{NSD} = \frac{\sqrt{\frac{1}{N}\sum_{i=1}^{N}(M_i-\overline{M})^2}}{\sqrt{\frac{1}{N}\sum_{i=1}^{N}(O_i-\overline{O})^2}}, \tag{5}$$

$$\mathrm{NRMSE} = \frac{\sqrt{\frac{1}{N}\sum_{i=1}^{N}((M_i-\overline{M})-(O_i-\overline{O}))^2}}{\sqrt{\frac{1}{N}\sum_{i=1}^{N}(O_i-\overline{O})^2}}, \tag{6}$$

where $M$ and $O$ denote the modelled and measured values, respectively; $\overline{M}$ and $\overline{O}$ represent their respective means; and $N$ is the total number of paired data. Collectively, these metrics provide a comprehensive evaluation of model performance: $R$ captures the ability to reproduce temporal and/or spatial variability; NSD indicates the relative magnitude of modelled variability compared to the observations; and NRMSE quantifies the overall deviation, normalised by the measured variability. Following the geometric relationship $\mathrm{NRMSE}^2 = 1 + \mathrm{NSD}^2 - 2 \cdot \mathrm{NSD} \cdot R$, these three metrics can be jointly visualised in a Taylor diagram (Taylor, 2001). In this coordinate system, $R$ is represented by the azimuthal angle, NSD by the radial distance from the origin, and NRMSE by the distance from the reference point (denoting perfect performance where $R = 1$ and $\mathrm{NSD} = 1$). Such a diagram offers an intuitive and concise framework to summarise and compare our evaluation results across both inversions and multiple temporal scales.

The three metrics described above, however, do not capture the overall bias between modelled and measured values. We therefore additionally define and visualize the normalized mean bias (NMB) on the same Taylor diagram to complement the

https://doi.org/10.5194/egusphere-2026-1499
Preprint. Discussion started: 1 April 2026


model evaluation:

$$\mathrm{NMB} = \frac{\sum_{i=1}^{N}(M_i - O_i)}{\sum_{i=1}^{N} O_i}. \tag{7}$$

From R and NSD, we further define an overall model skill metric (S) that combines both metrics as follows:

$$\mathrm{S} = \frac{4(1+\mathrm{R})}{(\mathrm{NSD}+1/\mathrm{NSD})^2(1+\mathrm{R}_0)}, \tag{8}$$

where $R_0$ represents the maximum achievable correlation coefficient given measurement uncertainties; for the purposes of this study, $R_0$ is set to 1. The resulting model skill score, $S$, ranges from 0 to 1, where a value of 1 signifies perfect agreement between modelled and observed values. We present this metric in a bar chart positioned beneath each Taylor diagram; together, these visualisations facilitate a robust comparison of the model performance yielded by the "GEMS-based" and "LEO-proxy" inversions.

## 3 Results and Discussion

### 3.1 Evaluation of updates to the adjoint of GEOS-Chem model

We investigate the capacity of GEMS geostationary tropospheric $NO_2$ observations to enhance $NO_x$ emission estimates and subsequent air quality modelling across a full annual cycle (December 2020 – November 2021). Our analysis reveals that the contrasts between the "GEMS-based" and "LEO-proxy" inversions primarily follow two distinct seasonal patterns: non-summer (September to May) and summer (June to August). To capture these patterns efficiently, we validate our adjoint model updates using two representative months: January and July 2021. For each representative month, we perform both a six-hour and a one-day simulation. The one-day simulation incorporates the full suite of GEMS retrievals, while the six-hour simulation subsets only those observations at 13:45 local time (KST) to serve as a LEO surrogate. This configuration ensures the validation conditions closely mirror the operational "GEMS-based" and "LEO-proxy" inversions. Figure 1 shows that the linear correlation coefficients and regression slopes between the adjoint-based and finite-difference-based sensitivities are nearly unity for both months and durations. These results verify the successful integration of contemporary emission inventories, aromatic chemistry, and new observation operators into the GEOS-Chem adjoint framework.

While accurate sensitivity computation is a prerequisite, the ultimate objective is the optimization of $NO_x$ emission scaling factors within the 4D-Var framework. Figure 2 presents an evaluation of the modelled tropospheric $NO_2$ columns against GEMS retrievals both before and after the optimisation. Although these evaluations are not independent, as the GEMS data are used for both constraint and evalution, they provide a necessary internal consistency check. We find that both inversions consistently reduce the model-observation mismatch across all months, with the most significant improvements observed during the non-summer (September to May) period. For instance, the overall model skill, $S$, has been improved by 0.47-208.65% and 0.32-200.36% during this period in the "GEMS-based" and "LEO-proxy" inversions, respectively. Despite the differing data densities between the "GEMS-based" and "LEO-proxy" experiments, the consistent performance enhancements demonstrate

https://doi.org/10.5194/egusphere-2026-1499
Preprint. Discussion started: 1 April 2026


that the updated adjoint model effectively optimises emissions. This successful evaluation provides the foundation for our subsequent assessment of the added value of GEMS geostationary observations of tropospheric $NO_2$ for $NO_x$ emission constraints and related air quality modelling.

### 3.2 Overall model evaluation against independent *in situ* measurements

Here we present the comprehensive model evaluation results against independent measurements of both columnar and surface $NO_2$ obtained from the *in situ* datasets detailed in Section 2.4. To complement this overarching evaluation, independent results for other chemical species within selected subregions are provided in Section 3.4. In that section, we further explore the contrasts in modelled atmospheric constituents between the "GEMS-based" and "LEO-proxy" inversions to quantify the added value of geostationary sampling.

Figure 3 shows the independent model evaluation results against columnar $NO_2$ measurements from AERONET. We observe that during the non-summer months (September to May), both inversions yield substantial improvements over the *a priori* simulation across all investigated temporal scales, including afternoon, daytime, and daily averages. Crucially, the model performance driven by $NO_x$ emissions from the "GEMS-based" inversion is generally superior or comparable to that of the "LEO-proxy" inversion. For instance, the largest improvements in the overall model skill, $S$, from the "LEO-proxy" inversion to the "GEMS-based" inversion occur in March or April, corresponding to 9.53%, 6.09%, and 5.02% increases in the afternoon, daytime, and daily-average evaluations, respectively. Conversely, during the summer months (June to August), the performance of both inversions degrades relative to the *a priori* simulation. In this period, the "GEMS-based" inversion performs slightly worse than the "LEO-proxy" counterpart. This seasonal discrepancy is also reflected in the independent validation against PGN columnar $NO_2$ measurements (Figure S5), although the limited number of PGN sites constrains the statistical robustness of these findings. To address this, we selected a specific site in Beijing characterised by high data coverage and more recent *a priori* emission data. The scatterplots of modelled versus measured columnar $NO_2$ at this site (Figure S6) further corroborate the contrasting patterns between the non-summer and summer periods identified in the broader PGN dataset.

Figures S7 and S8 show the independent model evaluation results against surface $NO_2$ measurements from CNEMC and CPCB, respectively. Consistent with the columnar evaluation, we observe a seasonal divide in China: both inversions yield performance improvements during the non-summer months (September to May) but result in degradations during the summer (June to August). Notably, the "GEMS-based" inversion exerts a more pronounced influence on the magnitude of these performance shifts compared to the "LEO-proxy" version. In contrast, model performance in India remains largely unchanged from the *a priori* simulation across all seasons and experiments. This lack of sensitivity is likely attributable to the lower density of GEMS tropospheric $NO_2$ retrievals over the Indian subcontinent relative to China (Figures S3, S4). For both the CNEMC and CPCB datasets, the model demonstrates higher skill when evaluated against daytime and daily averages rather than specific afternoon values. This suggests that high-frequency hourly measurements, which are not quality-screened, may contain stochastic noise that is effectively smoothed through temporal averaging. Furthermore, the relatively coarse spatial resolution of the model (2° latitude × 2.5° longitude) likely contributes to this trend, as temporal averaging helps mitigate the spatial representativeness mismatch between point-based *in situ* measurements and grid-averaged model values.

https://doi.org/10.5194/egusphere-2026-1499
Preprint. Discussion started: 1 April 2026


Ideally, a direct comparison between GEMS tropospheric $NO_2$ retrievals and *in situ* measurements would help reveal the factors driving the observed model degradation during summer. However, such an analysis is precluded by the absence of the requisite averaging kernels for both datasets, preventing a mathematically consistent comparison. We therefore speculate that the reduced model performance during the summer months is partly attributable to the markedly lower values of GEMS tropospheric $NO_2$ columns during summer than during non-summer months (Figures S9–S11), which are likely due to enhanced photochemical sinks. According to the GEMS $NO_2$ Algorithm Theoretical Basis Document (ATBD), retrieving such low concentrations is inherently more challenging, as slant column density errors increase significantly at low signal-to-noise ratios. This may lead to heightened uncertainties in GEMS retrievals during this period. Meanwhile, the contribution of non-anthropogenic sources to these low tropospheric $NO_2$ columns is likely higher, whereas our 4D-Var framework currently optimizes only anthropogenic emissions. Consequently, the "GEMS-based" inversion, which incorporates a larger volume of these uncertain retrievals, is more susceptible to these issues than the "LEO-proxy" inversion, potentially explaining its inferior performance in summer. The following sections focus on the non-summer months to assess the added value of geostationary sampling for constraining $NO_x$ emissions and modelling air quality.

### 3.3 Contrasts in inferred $NO_x$ emissions between GEMS–based and LEO–proxy inversions

Table 1 provides a summary of the adjustments made to the *a priori* $NO_x$ emissions by the "GEMS-based" and "LEO-proxy" inversions, alongside a comparison of their respective *a posteriori* estimates. Concentrating on the non-summer period (September to May), both inversions generally result in widespread increases in $NO_x$ emissions. However, the magnitude of these adjustments varies spatially and temporally; the "GEMS-based" estimates are either higher or lower than the "LEO-proxy" values depending on the specific region and month. For instance, Figure 4c1 and Figure S12c show that in April 2021, the "GEMS-based" inversion produces higher $NO_x$ emission estimates across much of East Asia, whereas the inverse is true over North India. This spatial divergence largely mirrors the differences in the distribution of the full GEMS dataset compared to the 13:45 KST subset (Figures 4c2 and S12i. This relationship is further confirmed by a statistically significant Pearson correlation coefficient ($R = 0.49$) between the differences in *a posteriori* emissions and the differences in GEMS retrievals (Figure 4c4). While the updates to a priori emissions primarily propagate linearly to modelled tropospheric $NO_2$ concentrations (Figure 4 a12, b12), some non-linearities persist. Consequently, the differences in modelled $NO_2$ between the two experiments (Figures 4c3 and S12f also align with the retrieval differences, showing a strong correlation of $R = 0.71$ (Figure 4c4). Although we omit a detailed discussion for every non-summer month for the sake of brevity, the significant month-to-month variability underscores the necessity of performing independent monthly inversions, as the results of one cannot serve as a direct proxy for another.

By aggregating $NO_x$ emissions over the pan-Asian region and categorising the contributions from areas where the "LEO-proxy" inversion either increases or decreases emissions, Figure 5 illustrates the monthly variations in adjustment patterns between the two experiments. Focusing on the non-summer period (September to May), both inversions yield widespread increases in $NO_x$ emissions across the domain. Consequently, the regionally aggregated $NO_x$ emissions (Figure 5c) are primarily driven by contributions from areas where the "LEO-proxy" inversion identified emission increases (Figure 5b). Consistent with

https://doi.org/10.5194/egusphere-2026-1499
Preprint. Discussion started: 1 April 2026


the summary in Table 1, the "GEMS-based" inversion produces higher total $NO_x$ emission estimates than the "LEO-proxy" inversion in March, May, and September, reflecting more uniformly robust upward adjustments across the region. Conversely, during other non-summer months, total emissions from the "GEMS-based" inversion are comparable to the "LEO-proxy" results, as the former applies a mixture of stronger and weaker upward adjustments depending on the sub-region. Overall, the aggregated pan-Asian $NO_x$ emissions from the two inversions differ by 0.2–52.6 GgN month$^{-1}$ during the non-summer months, representing 0.02–5.06% of the respective *a priori* totals. Although these regional differences appear modest, they represent bulk averages over a vast and heterogeneous domain; significantly larger contrasts emerge at finer spatial scales, as previously illustrated in Figures 4 and S12 and further explored in Section 3.4.

### 3.4 Contrasts in modelled atmospheric constituents between GEMS–based and LEO–proxy inversions

Following the analysis in Section 3.3, we maintain April 2021 as a representative month to illustrate the contrasts in modelled atmospheric composition resulting from the "GEMS-based" and "LEO-proxy" inversions. We examine several key constituents closely coupled to $NO_x$ emissions, specifically $NO_2$, $O_3$, OH, CO, HCHO, $SO_2$, $NH_3$, and secondary inorganic aerosols (sulfate, ammonium, and nitrate). For several of these species, independent *in situ* measurements are available to facilitate a rigorous performance evaluation.

Figure 6 demonstrates that the spatial hotspots of divergence in modelled constituents generally align with the spatial patterns of inferred $NO_x$ emission differences shown in Figures 4c1 and S12c. For instance, the "GEMS-based" inversion produces higher columnar and surface $NO_2$ concentrations across the North China Plain compared to the "LEO-proxy" inversion, while the inverse is observed over Northern India. Similar spatial distributions are evident for modelled HCHO and secondary inorganic aerosols, whereas CO and $NH_3$ exhibit reversed patterns. Interestingly, the "GEMS-based" inversion consistently yields higher $SO_2$ and lower $O_3$ and OH concentrations relative to the "LEO-proxy" inversion across the entire pan-Asian domain. These divergent responses reflect the complex, nonlinear atmospheric chemistry and coupling between $NO_x$ and other trace gases and aerosols. The sensitivity of these species varies significantly depending on the local chemical regime and ambient environmental conditions. For example, the uniform response of $O_3$ to different $NO_x$ adjustments in the North China Plain and Northern India highlights the contrasting VOC-limited and $NO_x$-limited regimes governing $O_3$ production in these respective regions.

We acknowledge that the contrasts in modelled atmospheric constituents between the two inversions are relatively modest for most species, typically within 10%, with surface-level changes being more pronounced than columnar adjustments. $NO_2$ is a notable exception, exhibiting changes of up to 20% in both columnar and surface concentrations. This is likely because $NO_2$ is more directly coupled to primary $NO_x$ emissions, whereas other species are influenced by a broader array of precursors and environmental factors. Consequently, the two inversions yield nearly identical model–observation biases for all non-$NO_2$ species and surface $NO_2$ (Figure S13). Nonetheless, the "GEMS-based" inversion does reduce model–observation biases for AERONET columnar $NO_2$ measurements relative to the "LEO-proxy" for most days in April 2021 over both the North China Plain and Northern India (Figure 7). Together with the overall model evaluation presented in Section 3.2, these results indicate that the "GEMS-based" inversion generally matches or exceeds the "LEO-proxy" inversion in improving model agreement

https://doi.org/10.5194/egusphere-2026-1499
Preprint. Discussion started: 1 April 2026


with independent *in situ* measurements during non-summer months, when retrievals are more robust. We therefore anticipate that other atmospheric constituents also benefit from the high-frequency constraints of the "GEMS-based" inversion; even where these differences appear small, such changes can have significant implications for health and environmental impact assessments.

To understand the added value of GEMS geostationary observations of tropospheric $NO_2$ for $NO_x$ emission constraints and subsequent air quality modelling during the non-summer months, we examine the diurnal variability of the observational part of the cost function ($J_{obs}$). Figure S14 illustrates an example for April 2021. Although $J_{obs}$ at 13:45 local time (KST) accounts for only a small fraction (12.1%) of the total $J_{obs}$, it correlates well with the total $J_{obs}$, with a Pearson correlation coefficient of 0.89. This indicates that the 13:45 KST retrievals, used in the "LEO-proxy" inversion, capture a substantial portion of the information content in the full GEMS dataset. Nevertheless, the remaining 87.9% of $J_{obs}$ from other hourly retrievals also contributes to the optimization process. The degree to which these additional observations differ from the 13:45 KST retrievals, and thus provide unique information, ultimately determines the added value of the GEMS geostationary sampling.

## 4 Conclusions

In this study, we rigorously assess the added value of GEMS geostationary satellite observations of tropospheric $NO_2$ for constraining $NO_x$ emissions and subsequent air quality modelling over a full annual cycle across the pan-Asian region. We conduct this assessment by comparing two 4D-Var inversion experiments using the GEOS-Chem adjoint model: a "GEMS-based" inversion assimilating the full hourly dataset and a "LEO-proxy" inversion utilising a subset of observations at 13:45 local time (KST) as a surrogate for Low Earth Orbit (LEO) data.

During the non-summer months (September to May), we find that both inversions yield widespread increases in $NO_x$ emissions. The "GEMS-based" estimates vary above or below "LEO-proxy" levels depending on the month and location, with spatial contrasts mirroring the differences in retrieval density between the full and single-overpass datasets. These adjustments propagate to several modelled atmospheric constituents, including $NO_2$, $O_3$, OH, CO, HCHO, $SO_2$, $NH_3$, and secondary inorganic aerosols, where divergent responses reflecting the complex, nonlinear atmospheric chemistry and coupling between $NO_x$ and these trace gases and aerosols. Independent evaluation against *in situ* columnar and surface $NO_2$ measurements confirms that the "GEMS-based" inversion generally matches or outperforms the "LEO-proxy" version during non-summer months, when retrievals are more robust. Conversely, during the summer (June to August), both inversions show degraded performance relative to the *a priori* simulation, likely due to increased retrieval uncertainties and stronger concentrations from non-anthropogenic $NO_x$ sources under extremely low $NO_2$ conditions that challenge the data assimilation framework in which only anthropogenic $NO_x$ sources are optimised.

To ensure a controlled comparison, we optimised only monthly total $NO_x$ emissions without adjusting their empirical temporal profiles. While this approach was necessary because the "LEO-proxy" lacks the temporal resolution to adjust diurnal profiles, it potentially underuses the high-frequency information available in the "GEMS-based" dataset. There are a few future directions that we hope to explore. First, adaptive error characterisation could be introduced by implementing dynamic obser-

https://doi.org/10.5194/egusphere-2026-1499
Preprint. Discussion started: 1 April 2026


vation error weighting to better leverage summer-time retrievals. Second, temporal profile optimisation could be achieved by jointly adjusting monthly totals and diurnal profiles to fully exploit geostationary sampling. Finally, employing finer resolution models would help to capture small-scale emission variability and urban-scale air quality impacts.

While previous studies have used geostationary data to investigate diurnal processes, few have quantified the long-term, domain-wide added value for emission constraints relative to LEO observations. By addressing this gap with the latest GEMS retrievals, our study provides critical insights into the benefits and technical challenges of integrating high-frequency satellite data into operational air quality management and policy-making frameworks.

*Code and data availability.* The adjoint of GEOS–Chem model is available from http://wiki.seas.harvard.edu/geos-chem/index.php/GEOS-Chem_Adjoint. The GEMS level–2 $NO_2$ product (v3.0) is available from the Environmental Satellite Center at the National Institute of Environmental Research (https://nesc.nier.go.kr/en/html/index.do).

*Author contributions.* FY and PIP designed the study. FY performed all model experiments and data analyses with contributions from XW and YW. HW assisted in acquiring the suite of *in situ* measurements. GTL and RJP guided the use of the GEMS tropospheric $NO_2$ data. LF and DKH assisted with the interpretation of the adjoint of GEOS–Chem model. FY and PIP wrote the manuscript with input from all authors.

*Competing interests.* The contact author has declared that none of the authors has any competing interests.

*Acknowledgements.* This research has been supported by the Natural Environment Research Council through the National Centre for Earth Observation (grant no. #NE/R016518/1).

https://doi.org/10.5194/egusphere-2026-1499
Preprint. Discussion started: 1 April 2026


## References

Bey, I., Jacob, D. J., Yantosca, R. M., Logan, J. A., Field, B. D., Fiore, A. M., Li, Q., Liu, H. Y., Mickley, L. J., and Schultz, M. G.: Global modeling of tropospheric chemistry with assimilated meteorology: Model description and evaluation, Journal of Geophysical Research: Atmospheres, 106, 23 073–23 095, 2001.

Boersma, K., Eskes, H., Veefkind, J., Brinksma, E., Van Der A, R., Sneep, M. v., Van Den Oord, G., Levelt, P., Stammes, P., Gleason, J., et al.: Near-real time retrieval of tropospheric NO 2 from OMI, Atmospheric Chemistry and Physics, 7, 2103–2118, 2007.

Byrd, R. H., Lu, P., Nocedal, J., and Zhu, C.: A limited memory algorithm for bound constrained optimization, SIAM Journal on scientific computing, 16, 1190–1208, 1995.

Cao, H., Henze, D. K., Shephard, M. W., Dammers, E., Cady-Pereira, K., Alvarado, M., Lonsdale, C., Luo, G., Yu, F., Zhu, L., et al.: Inverse modeling of NH3 sources using CrIS remote sensing measurements, Environmental Research Letters, 15, 104 082, 2020.

Choi, H., Park, S., Kang, Y., Im, J., and Song, S.: Retrieval of hourly PM2. 5 using top-of-atmosphere reflectance from geostationary ocean color imagers I and II, Environmental Pollution, 323, 121 169, 2023.

Choi, W. J., Moon, K.-J., Yoon, J., Cho, A., Kim, S.-k., Lee, S., Ko, D. h., Kim, J., Ahn, M. H., Kim, D.-R., et al.: Introducing the geostationary environment monitoring spectrometer, Journal of Applied Remote Sensing, 12, 044 005–044 005, 2018.

Crippa, M., Guizzardi, D., Muntean, M., Schaaf, E., Dentener, F., Van Aardenne, J. A., Monni, S., Doering, U., Olivier, J. G., Pagliari, V., et al.: Gridded emissions of air pollutants for the period 1970–2012 within EDGAR v4. 3.2, Earth Syst. Sci. Data, 10, 1987–2013, 2018.

Crippa, M., Guizzardi, D., Butler, T., Keating, T., Wu, R., Kaminski, J., Kuenen, J., Kurokawa, J., Chatani, S., Morikawa, T., et al.: The HTAP_v3 emission mosaic: merging regional and global monthly emissions (2000–2018) to support air quality modelling and policies, Earth system science data, 15, 2667–2694, 2023.

Deeter, M. N.: Calculation and application of MOPITT averaging kernels, National Center for Atmospheric Research (NCAR): Boulder, CO, 2002.

Edwards, D. P., Martínez-Alonso, S., Jo, D. S., Ortega, I., Emmons, L. K., Orlando, J. J., Worden, H. M., Kim, J., Lee, H., Park, J., et al.: Quantifying the diurnal variation in atmospheric NO 2 from Geostationary Environment Monitoring Spectrometer (GEMS) observations, Atmospheric Chemistry and Physics, 24, 8943–8961, 2024.

Fu, W., Zhu, L., Kwon, H.-A., Park, R. J., Lee, G. T., De Smedt, I., Liu, S., Li, X., Chen, Y., Pu, D., et al.: Evaluating GEMS HCHO retrievals with TROPOMI product, Pandora observations, and GEOS-Chem simulations, Earth and Space Science, 12, e2024EA003 894, 2025.

Guenther, A., Jiang, X., Heald, C. L., Sakulyanontvittaya, T., Duhl, T. a., Emmons, L., and Wang, X.: The Model of Emissions of Gases and Aerosols from Nature version 2.1 (MEGAN2. 1): an extended and updated framework for modeling biogenic emissions, Geoscientific Model Development, 5, 1471–1492, 2012.

Guizzardi, D., Crippa, M., Butler, T., Keating, T., Wu, R., Kamiński, J. W., Kuenen, J., Kurokawa, J., Chatani, S., Morikawa, T., et al.: The HTAP_v3. 1 emission mosaic: merging regional and global monthly emissions (2000–2020) to support air quality modelling and policies, Earth System Science Data Discussions, 2025, 1–49, 2025.

Gulde, S., Kolm, M., Smith, D., Maurer, R., Courrèges-Lacoste, G. B., Sallusti, M., and Bagnasco, G.: Sentinel 4: a geostationary imaging UVN spectrometer for air quality monitoring: status of design, performance and development, in: International Conference on Space Optics—ICSO 2014, vol. 10563, pp. 1158–1166, SPIE, 2017.

Hansen, P. C.: Rank-deficient and discrete ill-posed problems: numerical aspects of linear inversion, SIAM, 1998.

https://doi.org/10.5194/egusphere-2026-1499
Preprint. Discussion started: 1 April 2026


Henze, D. K., Hakami, A., and Seinfeld, J. H.: Development of the adjoint of GEOS-Chem, Atmospheric Chemistry and Physics, 7, 2413–2433, 2007.

Henze, D. K., Seinfeld, J. H., and Shindell, D. T.: Inverse modeling and mapping US air quality influences of inorganic PM 2.5 precursor emissions using the adjoint of GEOS-Chem, Atmospheric Chemistry and Physics, 9, 5877–5903, 2009.

Hoesly, R. M., Smith, S. J., Feng, L., Klimont, Z., Janssens-Maenhout, G., Pitkanen, T., Seibert, J. J., Vu, L., Andres, R. J., Bolt, R. M., et al.: Historical (1750–2014) anthropogenic emissions of reactive gases and aerosols from the Community Emissions Data System (CEDS), Geoscientific Model Development, 11, 369–408, 2018.

HYDE (2023); Gapminder (2022); UN WPP (2024) – with major processing by Our World in Data: "Population (historical)" [dataset], https://ourworldindata.org, sources: PBL Netherlands Environmental Assessment Agency, 'History Database of the Global Environment 3.3'; Gapminder, 'Population v7'; United Nations, 'World Population Prospects'; Gapminder, 'Systema Globalis' [original data].

Jung, J., Choi, Y., Souri, A. H., Mousavinezhad, S., Sayeed, A., and Lee, K.: The impact of springtime-transported air pollutants on local air quality with satellite-constrained NOx emission adjustments over East Asia, Journal of Geophysical Research: Atmospheres, 127, e2021JD035 251, 2022.

Kim, J., Jeong, U., Ahn, M.-H., Kim, J. H., Park, R. J., Lee, H., Song, C. H., Choi, Y.-S., Lee, K.-H., Yoo, J.-M., et al.: New era of air quality monitoring from space: Geostationary Environment Monitoring Spectrometer (GEMS), Bulletin of the American Meteorological Society, 101, E1–E22, 2020.

Kim, S., Kim, D., Hong, H., Chang, L.-S., Lee, H., Kim, D.-R., Kim, D., Yu, J.-A., Lee, D., Jeong, U., et al.: First-time comparison between NO 2 vertical columns from GEMS and Pandora measurements, Atmospheric Measurement Techniques Discussions, 2023, 1–22, 2023.

Lee, G. T., Park, R. J., Kwon, H.-A., Ha, E. S., Lee, S. D., Shin, S., Ahn, M.-H., Kang, M., Choi, Y.-S., Kim, G., et al.: First evaluation of the GEMS formaldehyde product against TROPOMI and ground-based column measurements during the in-orbit test period, Atmospheric Chemistry and Physics, 24, 4733–4749, 2024.

Letu, H., Yang, K., Nakajima, T. Y., Ishimoto, H., Nagao, T. M., Riedi, J., Baran, A. J., Ma, R., Wang, T., Shang, H., et al.: High-resolution retrieval of cloud microphysical properties and surface solar radiation using Himawari-8/AHI next-generation geostationary satellite, Remote Sensing of Environment, 239, 111 583, 2020.

Li, M., Zhang, Q., Kurokawa, J.-i., Woo, J.-H., He, K., Lu, Z., Ohara, T., Song, Y., Streets, D. G., Carmichael, G. R., et al.: MIX: a mosaic Asian anthropogenic emission inventory under the international collaboration framework of the MICS-Asia and HTAP, Atmospheric Chemistry and Physics, 17, 935–963, 2017.

Lucchesi, R.: File specification for GEOS-5 FP (Forward processing), Tech. rep., 2013.

Marvin, M. R., Palmer, P. I., Yao, F., Latif, M. T., and Khan, M. F.: Uncertainties from biomass burning aerosols in air quality models obscure public health impacts in Southeast Asia, Atmospheric Chemistry and Physics, 24, 3699–3715, 2024.

McDuffie, E. E., Smith, S. J., O'Rourke, P., Tibrewal, K., Venkataraman, C., Marais, E. A., Zheng, B., Crippa, M., Brauer, M., and Martin, R. V.: A global anthropogenic emission inventory of atmospheric pollutants from sector-and fuel-specific sources (1970–2017): an application of the Community Emissions Data System (CEDS), Earth System Science Data Discussions, 2020, 1–49, 2020.

Oak, Y. J., Jacob, D. J., Balasus, N., Yang, L. H., Chong, H., Park, J., Lee, H., Lee, G. T., Ha, E. S., Park, R. J., et al.: A bias-corrected GEMS geostationary satellite product for nitrogen dioxide using machine learning to enforce consistency with the TROPOMI satellite instrument, Atmospheric Measurement Techniques, 17, 5147–5159, 2024.

Park, J., Jung, J., Choi, Y., Lim, H., Kim, M., Lee, K., Lee, Y. G., and Kim, J.: Satellite-based, top-down approach for the adjustment of aerosol precursor emissions over East Asia: the TROPOspheric Monitoring Instrument (TROPOMI) NO 2 product and the Geostationary

https://doi.org/10.5194/egusphere-2026-1499
Preprint. Discussion started: 1 April 2026


Environment Monitoring Spectrometer (GEMS) aerosol optical depth (AOD) data fusion product and its proxy, Atmospheric Measurement Techniques, 16, 3039–3057, 2023.

Park, J., Choi, Y., Jung, J., Lee, K., and Yeganeh, A. K.: First top-down diurnal adjustment to NOx emissions inventory in Asia informed by the Geostationary Environment Monitoring Spectrometer (GEMS) tropospheric NO2 columns, Scientific Reports, 14, 24 338, 2024.

Park, J., Choi, Y., and Kayastha, S.: Local and transboundary contributions to NO y loadings across East Asia using CMAQ-ISAM and a GEMS-informed emission inventory during the winter–spring transition, Atmospheric Chemistry and Physics, 25, 4291–4311, 2025.

Price, C. and Rind, D.: A simple lightning parameterization for calculating global lightning distributions, Journal of Geophysical Research: Atmospheres, 97, 9919–9933, 1992.

Seo, S., Valks, P., Lutz, R., Heue, K.-P., Hedelt, P., Molina García, V., Loyola, D., Lee, H., and Kim, J.: Tropospheric NO2 retrieval algorithm for geostationary satellite instruments: applications to GEMS, Atmospheric Measurement Techniques, 17, 6163–6191, 2024.

Souri, A. H., Nowlan, C. R., González Abad, G., Zhu, L., Blake, D. R., Fried, A., Weinheimer, A. J., Wisthaler, A., Woo, J.-H., Zhang, Q., et al.: An inversion of NO x and non-methane volatile organic compound (NMVOC) emissions using satellite observations during the KORUS-AQ campaign and implications for surface ozone over East Asia, Atmospheric Chemistry and Physics, 20, 9837–9854, 2020.

Stephen, K. and Aneja, V. P.: Trends in agricultural ammonia emissions and ammonium concentrations in precipitation over the Southeast and Midwest United States, Atmospheric Environment, 42, 3238–3252, 2008.

Tang, Z., Jiang, Z., Chen, J., Yang, P., and Shen, Y.: The capabilities of the adjoint of GEOS-Chem model to support HEMCO emission inventories and MERRA-2 meteorological data, Geoscientific Model Development, 16, 6377–6392, 2023.

Taylor, K. E.: Summarizing multiple aspects of model performance in a single diagram, Journal of geophysical research: atmospheres, 106, 7183–7192, 2001.

Van Der Werf, G. R., Randerson, J. T., Giglio, L., Van Leeuwen, T. T., Chen, Y., Rogers, B. M., Mu, M., Van Marle, M. J., Morton, D. C., Collatz, G. J., et al.: Global fire emissions estimates during 1997–2016, Earth System Science Data, 9, 697–720, 2017.

Veefkind, J. P., Aben, I., McMullan, K., Förster, H., De Vries, J., Otter, G., Claas, J., Eskes, H., De Haan, J., Kleipool, Q., et al.: TROPOMI on the ESA Sentinel-5 Precursor: A GMES mission for global observations of the atmospheric composition for climate, air quality and ozone layer applications, Remote sensing of environment, 120, 70–83, 2012.

Wang, J., Xu, X., Henze, D. K., Zeng, J., Ji, Q., Tsay, S.-C., and Huang, J.: Top-down estimate of dust emissions through integration of MODIS and MISR aerosol retrievals with the GEOS-Chem adjoint model, Geophysical research letters, 39, 2012.

Wang, X., Fu, T.-M., Zhang, L., Cao, H., Zhang, Q., Ma, H., Shen, L., Evans, M. J., Ivatt, P. D., Lu, X., et al.: Sensitivities of ozone air pollution in the Beijing–Tianjin–Hebei area to local and upwind precursor emissions using adjoint modeling, Environmental Science & Technology, 55, 5752–5762, 2021.

Wang, Y., Wang, J., Xu, X., Henze, D. K., Wang, Y., and Qu, Z.: A new approach for monthly updates of anthropogenic sulfur dioxide emissions from space: Application to China and implications for air quality forecasts, Geophysical Research Letters, 43, 9931–9938, 2016.

Wang, Y., Wang, J., Xu, X., Henze, D. K., Qu, Z., and Yang, K.: Inverse modeling of SO 2 and NO x emissions over China using multisensor satellite data–Part 1: formulation and sensitivity analysis, Atmospheric Chemistry and Physics, 20, 6631–6650, 2020.

Xu, J.-W., Martin, R., Van Donkelaar, A., Kim, J., Choi, M., Zhang, Q., Geng, G., Liu, Y., Ma, Z., Huang, L., et al.: Estimating ground-level PM 2.5 in eastern China using aerosol optical depth determined from the GOCI satellite instrument, Atmospheric Chemistry and Physics, 15, 13 133–13 144, 2015.

https://doi.org/10.5194/egusphere-2026-1499
Preprint. Discussion started: 1 April 2026


Xu, T., Zhang, C., Xue, J., Hu, Q., Xing, C., and Liu, C.: Estimating hourly nitrogen oxide emissions over East Asia from geostationary satellite measurements, Environmental Science & Technology Letters, 11, 122–129, 2023.

Xu, X., Wang, J., Henze, D. K., Qu, W., and Kopacz, M.: Constraints on aerosol sources using GEOS-Chem adjoint and MODIS radiances, and evaluation with multisensor (OMI, MISR) data, Journal of Geophysical Research: Atmospheres, 118, 6396–6413, 2013.

Yang, K., Dickerson, R. R., Carn, S. A., Ge, C., and Wang, J.: First observations of SO2 from the satellite Suomi NPP OMPS: Widespread air pollution events over China, Geophysical Research Letters, 40, 4957–4962, 2013.

Yang, K., Carn, S. A., Ge, C., Wang, J., and Dickerson, R. R.: Advancing measurements of tropospheric NO2 from space: New algorithm and first global results from OMPS, Geophysical Research Letters, 41, 4777–4786, 2014.

Yang, L. H., Jacob, D. J., Dang, R., Oak, Y. J., Lin, H., Kim, J., Zhai, S., Colombi, N. K., Pendergrass, D. C., Beaudry, E., et al.: Interpreting Geostationary Environment Monitoring Spectrometer (GEMS) geostationary satellite observations of the diurnal variation in nitrogen dioxide (NO 2) over East Asia, Atmospheric Chemistry and Physics, 24, 7027–7039, 2024.

Yeom, J.-M., Roujean, J.-L., Han, K.-S., Lee, K.-S., and Kim, H.-W.: Thin cloud detection over land using background surface reflectance based on the BRDF model applied to Geostationary Ocean Color Imager (GOCI) satellite data sets, Remote Sensing of Environment, 239, 111 610, 2020.

Yienger, J. and Levy, H.: Empirical model of global soil-biogenic NO$\chi$ emissions, Journal of Geophysical Research: Atmospheres, 100, 11 447–11 464, 1995.

Zara, M., Boersma, K. F., De Smedt, I., Richter, A., Peters, E., Van Geffen, J. H., Beirle, S., Wagner, T., Van Roozendael, M., Marchenko, S., et al.: Improved slant column density retrieval of nitrogen dioxide and formaldehyde for OMI and GOME-2A from QA4ECV: inter-comparison, uncertainty characterisation, and trends, Atmospheric Measurement Techniques, 11, 4033–4058, 2018.

Zheng, B., Tong, D., Li, M., Liu, F., Hong, C., Geng, G., Li, H., Li, X., Peng, L., Qi, J., et al.: Trends in China's anthropogenic emissions since 2010 as the consequence of clean air actions, Atmospheric Chemistry and Physics, 18, 14 095–14 111, 2018.

Zheng, B., Zhang, Q., Geng, G., Chen, C., Shi, Q., Cui, M., Lei, Y., and He, K.: Changes in China's anthropogenic emissions and air quality during the COVID-19 pandemic in 2020, Earth System Science Data, 13, 2895–2907, 2021.

Zoogman, P., Liu, X., Suleiman, R., Pennington, W., Flittner, D., Al-Saadi, J., Hilton, B., Nicks, D., Newchurch, M., Carr, J., et al.: Tropospheric emissions: Monitoring of pollution (TEMPO), Journal of Quantitative Spectroscopy and Radiative Transfer, 186, 17–39, 2017.

https://doi.org/10.5194/egusphere-2026-1499
Preprint. Discussion started: 1 April 2026


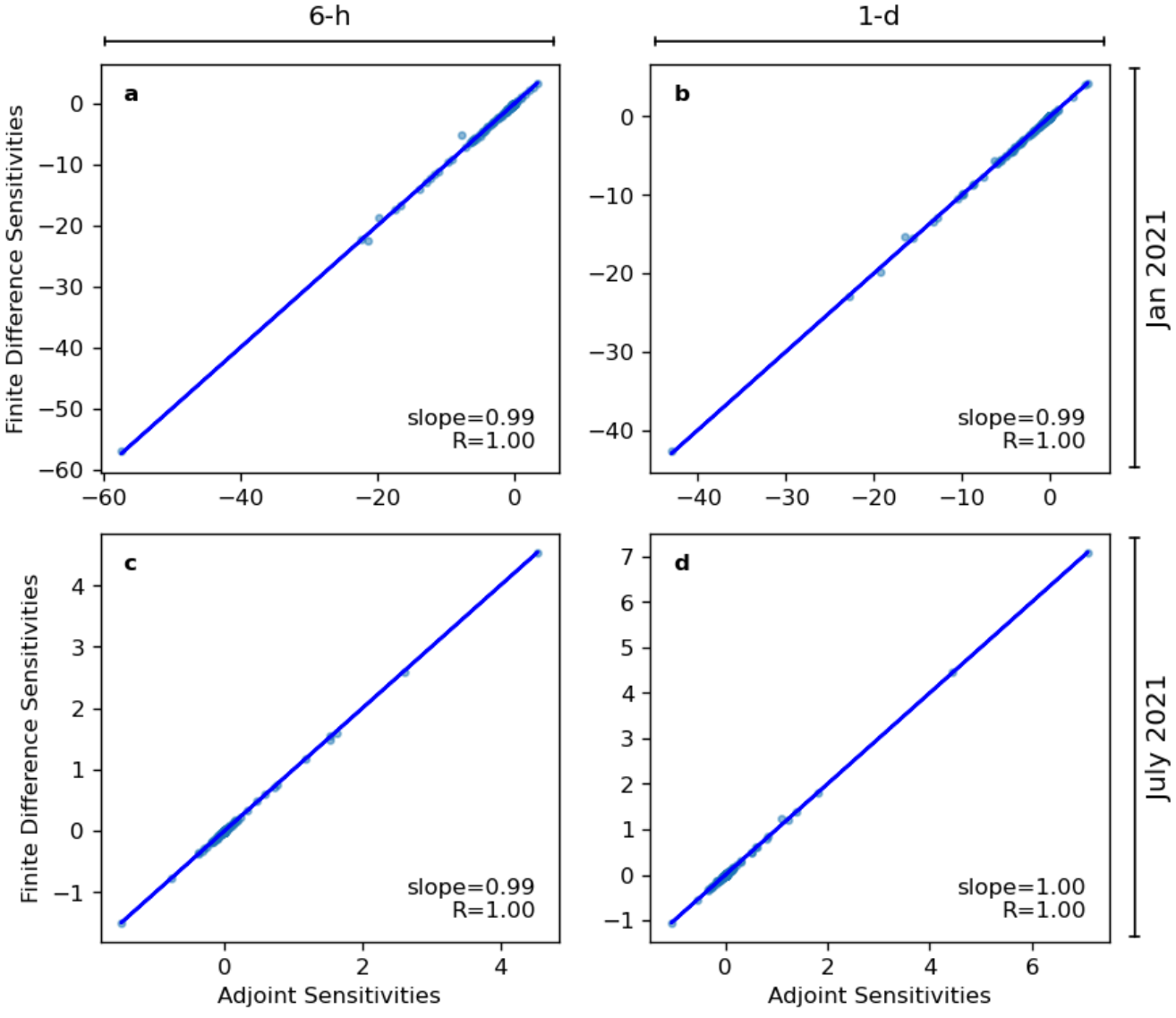


**Figure 1.** Evaluation of updates to the adjoint of GEOS–Chem model by comparing adjoint–based and finite–difference–based sensitivities of the cost function (penalty term is excluded, and horizontal transport is turned off) with respect to logarithmic scaling factors of $NO_x$ emissions for for January (**a**, **b**) and July (**c**, **d**) 2021 with a six–hour simulation including only GEMS tropospheric $NO_2$ retrievals at 13:45 local time (Korea Standard Time) (**a**, **c**) and with a one–day simulation including all available GEMS tropospheric $NO_2$ retrievals for that day (**b**, **d**). The linear correlation coefficients (R) and linear regression slopes between the two sets of sensitivities are also shown in each panel.

https://doi.org/10.5194/egusphere-2026-1499
Preprint. Discussion started: 1 April 2026


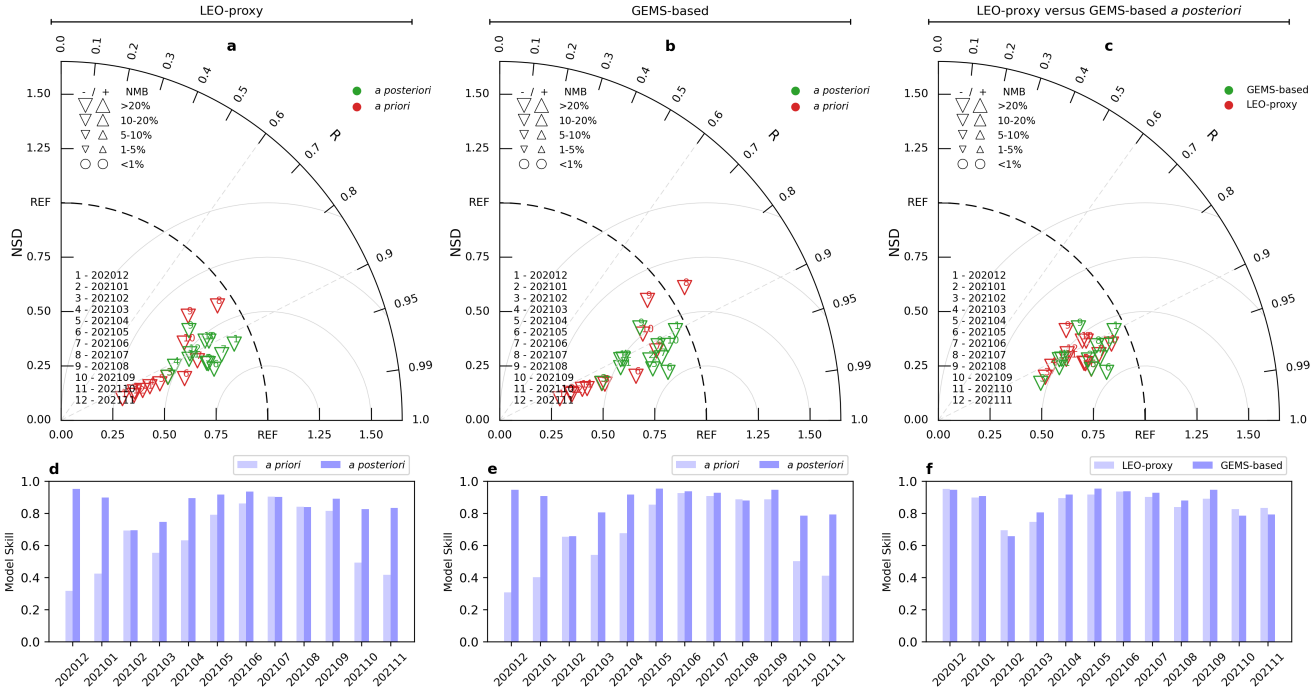


**Figure 2.** Non-independent model evaluation for the "LEO-proxy" (**a**, **d**) and "GEMS-based" (**b**, **e**) inversions, and a comparison between them (**c**, **f**). Each point on the taylor diagram (**a**–**c**) represents the Pearson correlation coefficient (R), normalized standard deviation (NSD), normalized centered root-mean-square error (NRMSE), and normalized mean bias (NMB) between modelled and satellite-retrieved tropospheric $NO_2$, which are interpreted by the azimuthal angle (R), radial distance from the origin (NSD), distance from the reference (REF) point (NRMSE), and the marker shape and size (NMB), respectively. The points distinguish between *a priori* (red) and *a posteriori* (green) model simulations in panels **a** and **b**, as well as between the "LEO-proxy" (red) and "GEMS-based" (green) *a posteriori* simulations in panel **c**. Each vertical bar in panels **d**–**f** shows the model skill before and after the "LEO-proxy" and "GEMS-based" inversions, as well as a comparison between their *a posteriori* model skill.

https://doi.org/10.5194/egusphere-2026-1499
Preprint. Discussion started: 1 April 2026


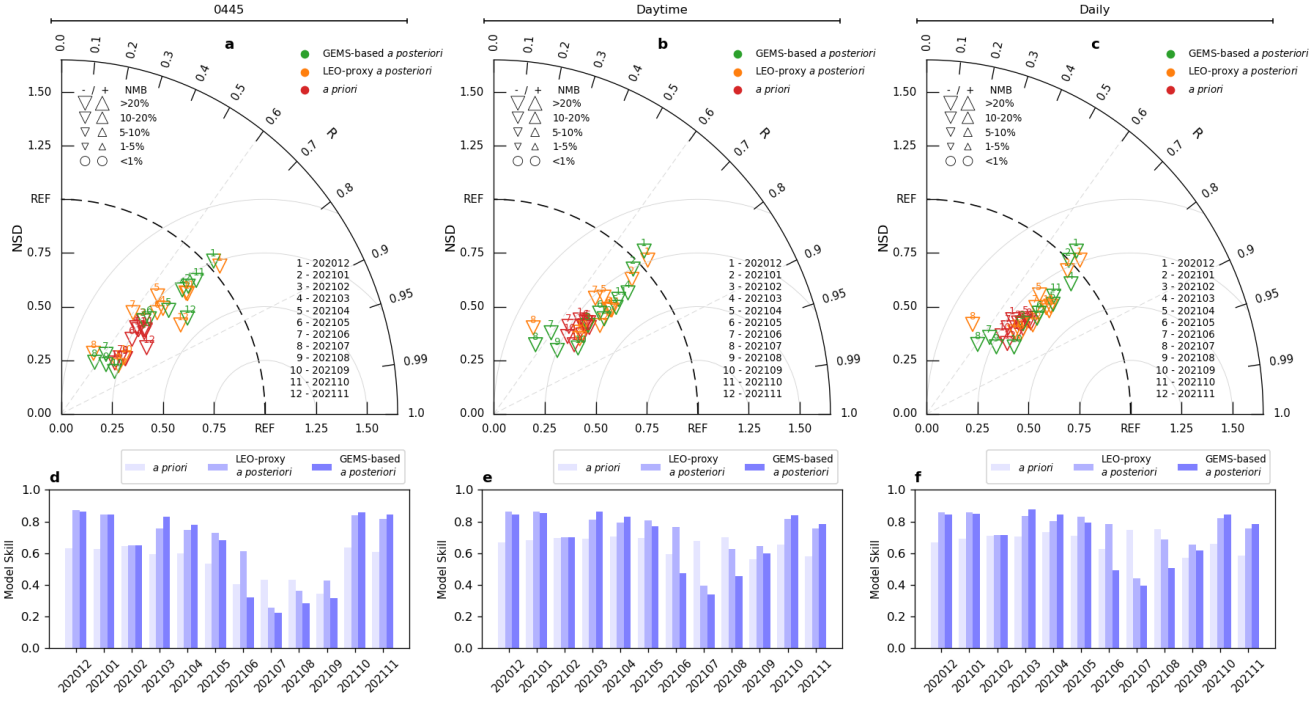


**Figure 3.** Independent model evaluation against columnar $NO_2$ measurements from the Aerosol Robotic Network (AERONET) for the "LEO–proxy" and "GEMS–based" inversions across multiple temporal scales, including the afternoon overpass at 13:45 local time (Korea Standard Time) (**a**, **d**), daytime averages (07:45 to 16:45 KST) (**b**, **e**), and full daily averages (**c**, **f**). The interpretation of the Taylor diagrams (**a**–**c**) and model skill bar charts (**d**–**f**) is the same as that described in the caption of Figure 2, except that here we distinguish the *a priori*, "LEO–proxy" *a posteriori*, and "GEMS–based" *a posteriori* model simulations on each of the Taylor diagrams and model skill bar charts.

https://doi.org/10.5194/egusphere-2026-1499
Preprint. Discussion started: 1 April 2026


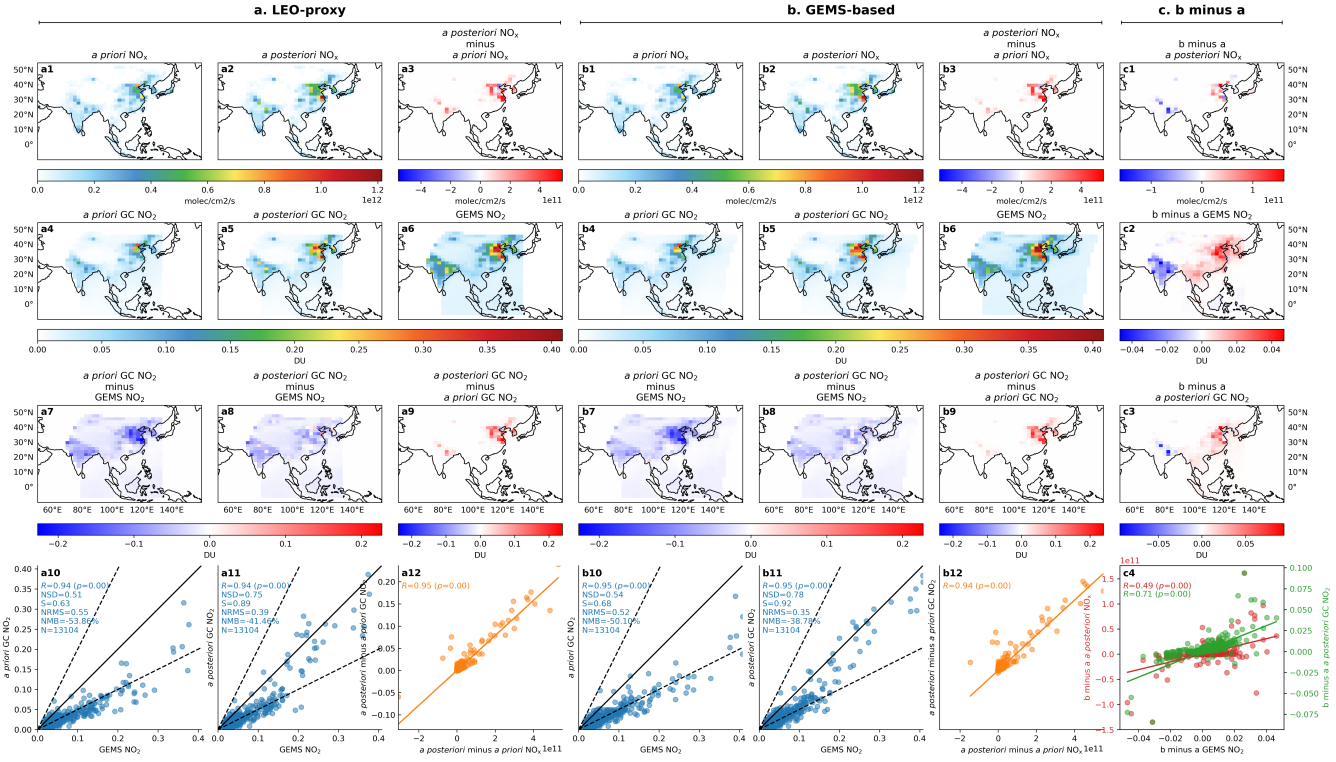


**Figure 4.** Results for April 2021 from the "LEO–proxy" (**a1**–**a12**) and "GEMS–based" (**b1**–**b12**) inversions, along with a comparison between them (**c1**–**c4**). For each inversion, we show: the *a priori* $NO_x$ emissions (**a1**, **b1**) and *a posteriori* $NO_x$ emissions (**a2**, **b2**), their differences (**a3**, **b3**), modelled tropospheric $NO_2$ based on *a priori* (**a4**, **b4**) and *a posteriori* (**a5**, **b5**) $NO_x$ emissions and the associated changes from *a priori* to *a posteriori* (**a9**, **b9**), the differences between modelled and GEMS tropospheric $NO_2$ (**a6**, **b6**) for *a priori* (**a7**, **b7**) and *a posteriori* (**a8**, **b8**) values, scatter plots of modelled versus GEMS tropospheric $NO_2$ for *a priori* (**a10**, **b10**) and *a posteriori* (**a11**, **b11**) values, and finally scatter plots of the differences between *a posteriori* and *a priori* modelled tropospheric $NO_2$ and $NO_x$ (**a12**, **b12**). For comparing the two inversions, we show the differences between their *a posteriori* $NO_x$ emissions (**c1**) and the subsequently modelled $NO_2$ (**c3**) alongside the corresponding GEMS tropospheric $NO_2$ (**c2**), as well as scatter plots of the differences in modelled tropospheric $NO_2$ and $NO_x$ between the two inversions versus the corresponding differences in GEMS tropospheric $NO_2$ retrievals (**c4**). For panels **a3, b3, c1, a9, b9, c3, a8, b8, c2**, we show their respective percentage changes in Figure S12.

https://doi.org/10.5194/egusphere-2026-1499
Preprint. Discussion started: 1 April 2026


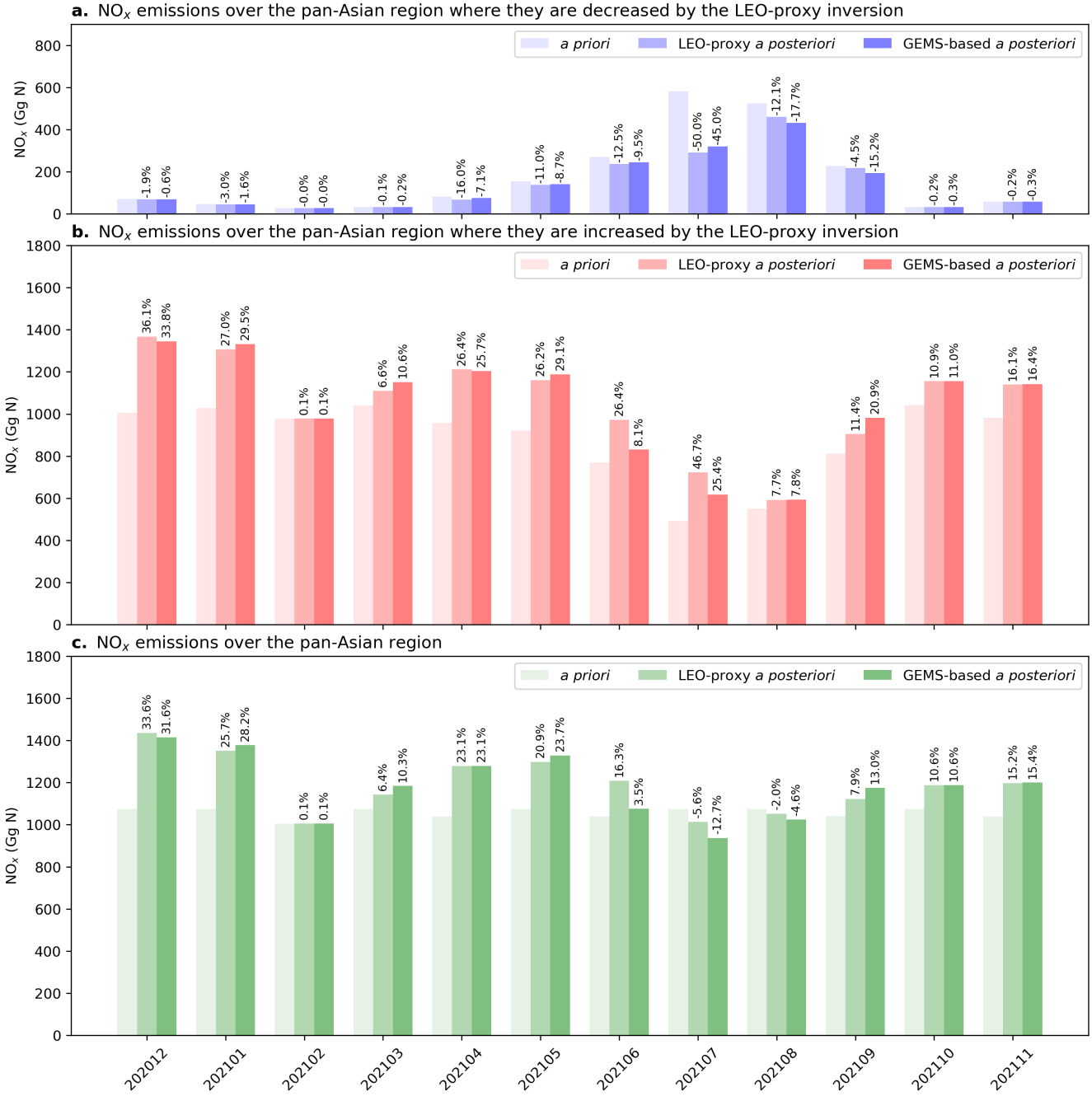


**Figure 5.** $NO_x$ emissions, expressed in Gg N, aggregated over the pan–Asian region (**c**) and their components corresponding to the areas where they are decreased (**a**) and increased (**b**) by the "LEO–proxy" inversion, respectively.

https://doi.org/10.5194/egusphere-2026-1499
Preprint. Discussion started: 1 April 2026


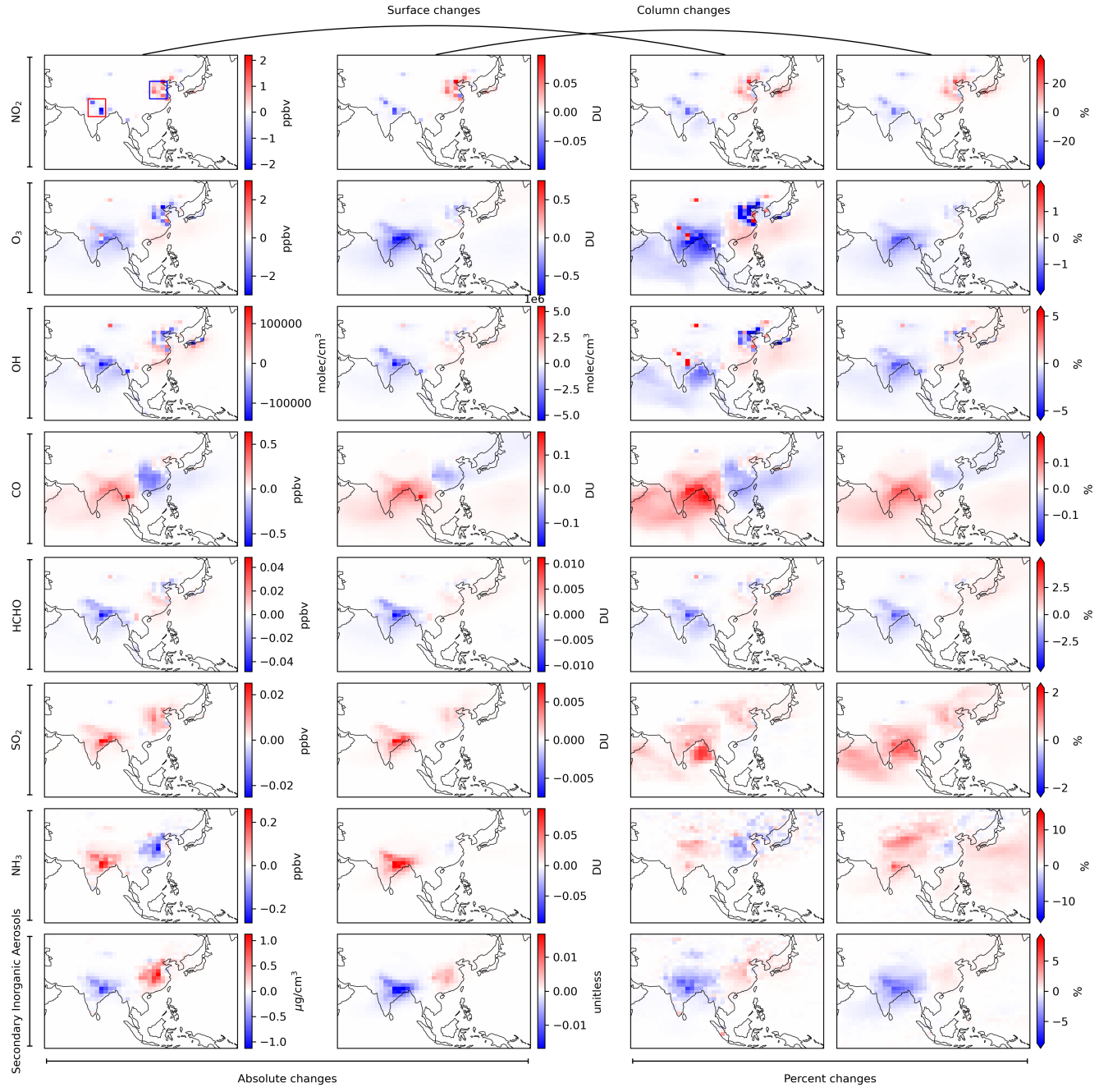


**Figure 6.** Absolute and percentage differences between column and surface concentrations of modelled atmospheric constituents ($NO_2$, $O_3$, OH, CO, HCHO, $SO_2$, $NH_3$, and secondary inorganic aerosols) as driven by the "LEO–proxy" and "GEMS–based" inversions in April 2021. The blue and red rectangles in the top-left panel highlight two areas where the contrasts between the two inversions are most pronounced, referred to here as the "North China Plain" and "Northern India" subregions, respectively.

https://doi.org/10.5194/egusphere-2026-1499
Preprint. Discussion started: 1 April 2026


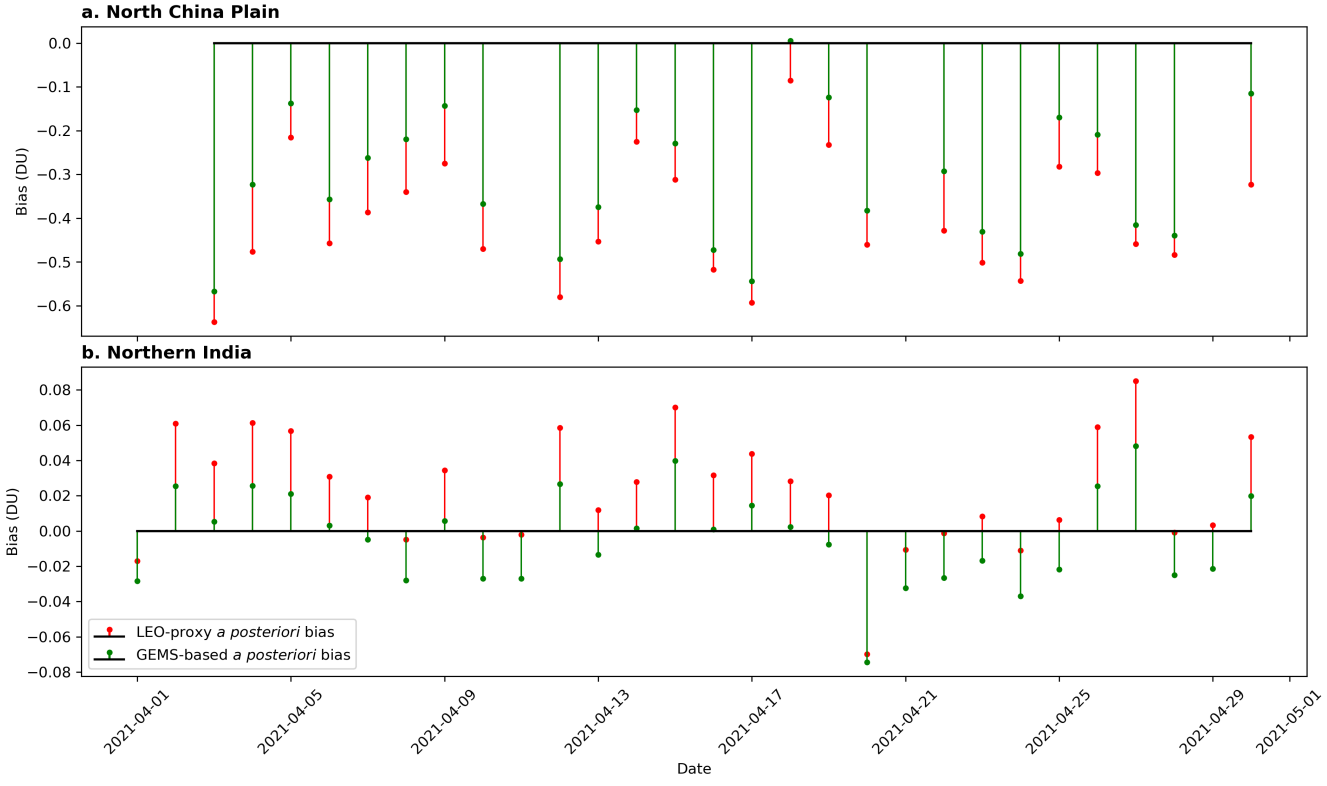


**Figure 7.** Stem plot of model–observation biases in column $NO_2$ over the North China Plain and Northern India subregions in April 2021.

https://doi.org/10.5194/egusphere-2026-1499
Preprint. Discussion started: 1 April 2026


**Table 1.** Comparisons of the "LEO–proxy" and "GEMS–based" *a posteriori* $NO_x$ emission estimates relative to the *a priori* $NO_x$ emissions, along with a comparison between their *a posteriori* $NO_x$ emission estimates.

| Month | *a posteriori* versus *a priori* $NO_x$ emissions | LEO–proxy versus GEMS–based *a posteriori* $NO_x$ emission estimates |
|---|---|---|
| 202012 | Widespread increases in $NO_x$ emissions | GEMS–based results can be higher or lower than those of LEO–proxy depending on location |
| 202101 | Widespread increases in $NO_x$ emissions | GEMS–based results can be higher or lower than those of LEO–proxy depending on location |
| 202102 | Widespread increases in $NO_x$ emissions | GEMS–based results can be higher or lower than those of LEO–proxy depending on location |
| 202103 | Widespread increases in $NO_x$ emissions | GEMS–based results are higher than those of LEO–proxy across the pan-Asian region |
| 202104 | Widespread increases in $NO_x$ emissions | GEMS–based results can be higher or lower than those of LEO–proxy depending on location |
| 202105 | Widespread increases in $NO_x$ emissions | GEMS–based results are higher than those of LEO–proxy across the pan-Asian region |
| 202106 | Widespread increases in $NO_x$ emissions | GEMS–based results are lower than those of LEO–proxy across the pan-Asian region |
| 202107 | Mixed increases and decreases in $NO_x$ emissions | GEMS–based results are more conservative as compared to those of LEO–proxy |
| 202108 | Mixed increases and decreases in $NO_x$ emissions | GEMS–based results are more pronounced as compared to those of LEO–proxy |
| 202109 | Widespread increases in $NO_x$ emissions | GEMS–based results are higher than those of LEO–proxy across the pan-Asian region |
| 202110 | Widespread increases in $NO_x$ emissions | GEMS–based results can be higher or lower than those of LEO–proxy depending on location |
| 202111 | Widespread increases in $NO_x$ emissions | GEMS–based results can be higher or lower than those of LEO–proxy depending on location |